Enhancing Human-Robot Collaboration: Supernumerary Robotic Limbs for Object Balance

Jing Luo, *Member, IEEE,* Shiyang Liu, *Student Member, IEEE,*
Weiyong Si, *Member, IEEE,* Chao Zeng, *Member, IEEE*

Abstract—Supernumerary Robotic Limb (SRL) is recognized as being at the forefront of robotics innovation, aimed at augmenting human capabilities in complex working environments. Despite their potential to significantly enhance operational efficiency, the integration of SRL for dynamic and intricate tasks presents challenges in teleoperation, precise positioning, and dynamic balance control. To address challenges in initiating control when targets or the SRL's end-effector are outside the camera's visual range, a coarse teleoperation strategy is implemented. This strategy utilizes Inertial Measurement Unit (IMU) and the Extended Kalman Filter (EKF), enabling basic orientation and movement toward the target area without reliance on visual cues. Challenges in achieving fine-tuned control for accurate task completion, particularly in visual navigation and precise positioning of the SRL's end-effector, are addressed by integrating object detection via YOLOX with the Tangential Artificial Potential Field (T-APF) method for exact path planning. This integration significantly enhances the system's ability to fine-tune end-effector placement. The challenge of conducting balance tasks without force sensors is tackled by adopting a dual-spring model combined with Autoregressive (AR) predictive modeling, enabling effective balance support through anticipatory motion adjustments. Experiments have demonstrated the system's enhanced positional accuracy and maintained synchronization with human movements, underscoring the effectiveness of the integrated approach in facilitating complex human-robot collaborative tasks.

Index Terms—Supernumerary Robotic Limbs, Teleoperation, Vision-Enhanced Positioning, Human-Robot Collaboration.
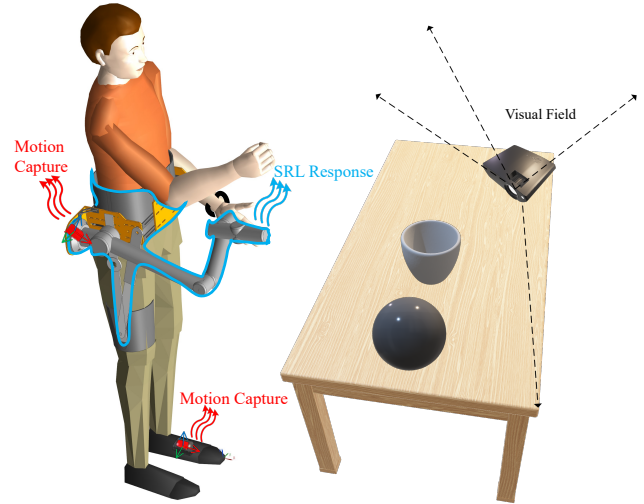
Fig. 1: The cartoon showcase of the human-SRL system. The designed SRL is mounted at the right waist side of the operator, establishing a rigid connection with the operator via attachment points on the leg and a waist belt. To capture the operator's teleoperation intentions and monitor the real-time posture changes of the SRL, two IMU are positioned on both the operator's dorsum of the foot and the base of the SRL. Additionally, a Kinect V1 is mounted on a desk within proximity to the operation area, whose field of view covers the operator's working zone.

I. Introduction

IN recent years, the robotics landscape has undergone transformative advancements, most notably in the specialized area of Supernumerary Robotic Limbs (SRL) [1]. These innovative robotic systems are engineered to augment and emulate human limb movements without supplanting them, thereby unlocking new possibilities in diverse fields such as assistive technologies and advanced manufacturing [2]. SRL possess the unique capability to function in synchrony with human limbs,

achieving seamless integration of human intuition and robotic precision.

Initial research in the field of SRL primarily focused on mechanical design and preliminary control algorithms, as highlighted by Bonilla *et al.* [3]. Early explorations, such as those by Abdi *et al.*, investigated the use of foot movements to control a third robotic hand in virtual reality, emphasizing the potential of SRL as extensions of the human body with key design principles of safety, transparency, and ergonomic comfort [4]. With the evolution of SRL technology, there is an increasing emphasis on advanced control mechanisms that integrate human intentions with robotic actions, although the technology remains largely experimental [5]. Hussain *et al.* introduced an electromyographic (EMG) control interface for a supernumerary robotic finger's motion and joint compliance, exemplifying such advancements [6]. Wu *et al.* presented a control algorithm for human fingers and supernumerary robotic fingers to share loads [29]. Hao *et al.* designed an SRL system with robotic legs for walking assistance, reducing user load through autonomous gait alignment [30]. Kurek *et al.* introduced a wearable device with two robotic legs

Jing Luo is with School of Automation, Wuhan University of Technology, Wuhan, China, and also with Chongqing Research Institute, Wuhan University of Technology, Chongqing, China. (e-mail: jingluo@ieee.org)

Shiyang Liu is with School of Automation, Wuhan University of Technology, Wuhan, China. (e-mail: stefanlov1ez@gmail.com)

Weiyong Si is with School of Computer Science and Electronic Engineering, University of Essex, Essex, U.K. (e-mail: w.si@essex.ac.uk)

Chao Zeng is with the Department of Informatics, University of Hamburg, Hamburg, Germany. (e-mail: chaozeng@ieee.org)

for ground-level tasks, eliminating the need for arm support through impedance control for stability [31]. The evolution of SRL from mechanical designs to advanced control systems showcases a broadening of applicationsfrom enhancing dexterity with robotic fingers and hands, facilitating load sharing, to improving mobility with robotic legs. Each development iteratively refines SRL' integration with human capabilities, distinguishing between augmenting upper body tasks for manual assistance and lower body support for mobility and balance.

SRL have significantly evolved from augmenting basic human functions to addressing complex biomechanical challenges, as highlighted in early works such as the wearable additional arms developed by Davenport *et al.* [18]. The focus of SRL development has expanded from foundational concepts and biomechanics to multipurpose use and wearability, evidenced by the shape-changing SRL by Leigh *et al.* [19] and the serpentine robot by Al-Sada *et al.* [20]. However, a critical area for further exploration in SRL is advanced target detection, vital for performing complex tasks. While the field has made strides in human augmentation and implications on body schema, as explored by Tsakiris *et al.* through the rubber hand illusion [22], and in soft wearable assistive robotics for operator comfort, as demonstrated by Iwaki *et al.* [24] and Treers *et al.* [25], integrating advanced functionalities like precise target detection remains an uncharted territory. This gap highlights the necessity for continued research to not only enhance the mechanical and ergonomic aspects of SRL but also to incorporate sophisticated technologies for their effective application in varied and complex operational environments. However, a significant ongoing challenge is the precise prediction and replication of human motion, where conventional methods often lack the finesse and real-time responsiveness required for more complex tasks [26].

In addressing the precision challenges inherent in robotics and SRL, the integration of Inertial Measurement Unit (IMU) and Extended Kalman Filter (EKF) emerges as a prominent solution within the research community [7], [8]. IMU, celebrated for their compact size and high accuracy in capturing motion data, is crucial for estimating spatial orientation and position despite susceptibility to drift errors over extended periods. EKF counters these inaccuracies, offering dynamic system state estimation from noisy IMU data, thereby enhancing motion estimation accuracy. This approach is augmented by sensor fusion techniques, where IMU data is combined with other sensors like Ultra-Wideband (UWB) and 3D Lidar, to achieve robust localization and control [9]–[12]. Such integrations underscore the potential of sophisticated computational algorithms and diverse sensor modalities in advancing the operational efficiency and accuracy of complex robotic systems, including SRL [27], [28].

Despite these significant strides, a gap persists in enabling SRL to proactively adapt to abrupt changes in human motion. Lehrmann *et al.* applied Autoregressive (AR) model prediction in human motion [13]. These models facilitate real-time trajectory adjustments by forecasting human motion, thereby ensuring synchronized robotic operations. For example, Maurice *et al.* compiled a dataset of human motions

in industrial-like settings, providing a valuable resource for algorithm development in human motion prediction [14]. Luo *et al.* formulated a human motion intention prediction method based on an AR model for teleoperation, allowing for real-time trajectory updates [15].

In the dynamic context of SRL applications, essential functionalities such as target detection have become imperative for executing complex services. For instance, in grasp-oriented tasks, the operator needs to accurately identify and interact with target objects, necessitating advanced detection mechanisms by the external limbs. However, current research on target detection and related functionalities within the SRL domain remains limited [5]. This gap highlights the necessity for focused research and development in areas critical to the operational effectiveness of SRL, such as sensor integration, motion prediction, and real-time adaptability to complex scenarios. This study, therefore, assumes significant relevance, as it seeks to address these challenges and extend the scope of SRL technology. By integrating enhanced control mechanisms and predictive models, this work aims to facilitate a more intuitive and efficient human-robot interaction, marking a step towards revolutionizing SRL applications and integrating them seamlessly into real-world scenarios.

Recognizing the challenges in enhancing the functionality and applicability of SRL in complex service scenarios, particularly in target detection and interaction tasks, this study proposes several innovative solutions to bridge these gaps. To address the pressing need for advanced detection and interaction mechanisms in SRL applications, our research contributions are summarized as follows:

1) Development of a target detection and tracking system: Advanced sensor technology and deep learning algorithms are leveraged to enhance the SRL's object identification and interaction in various environments, boosting task efficiency.

2) Integration of predictive modeling for dynamic interaction: Incorporating AR predictive models allows the SRL system to foresee human movements and adapt in real-time, improving human-robot collaboration.

3) Real-time adaptive control mechanism: IMU inputs and vision feedback are used to dynamically adapt to changing operational conditions, ensuring precise and responsive manipulation.

The structure of this paper is organized as follows: Related work is reviewed in Section II. Then, an overview of the methodologies utilized is provided in Section III, detailing the innovative approaches for controlling SRL. The methodology comprises: EKF and IMU-Based coarse teleoperation in Section IIIA, vision-based fine positioning in Section IIIB, and deformation estimation for object balance detailed in Section IIIC. Experimental results and comprehensive discussion are presented in Section IV. The paper is concluded in Section VI.

II. RELATED WORK

A. IMU-Based Position Prediction

IMU play a key role in enhancing teleoperation and SRL control through real-time orientation and position measurement, especially for precise control and synchronization. Zhu

et al. developed an IMU-based system to attenuate arm tremors in teleoperation [41], while kulj *et al.* introduced a wearable IMU system for industrial robot teleoperation, focusing on real-time orientation data [33]. Expanding upon real-time data utilization, Li *et al.* combined vision and IMU techniques for accurate anthropomorphic hand joint angle predictions [34]. Weigend *et al.* used IMU data from a smartwatch for human arm pose deductions, offering accessible robot control solutions [35]. Girbs-Juan *et al.* integrated haptic feedback with IMU-based motion capture for remote dual-arm robot control [36]. Tortora *et al.* combined EMG with IMU data for enhanced human-robot synchronization [37].

These studies underscore the potential of IMU-based systems in enhancing the precision and reliability of teleoperation systems, especially in scenarios where real-time feedback and synchronization are paramount. Inspired by these advancements, our work focuses on applying IMU-based teleoperation methods to the SRL platform. Our aim is to validate the feasibility of these methods on SRL and to address the unique challenges or optimizations required for this specific task.

B. Advanced Path Planning: Integrating Object Detection with Artificial Potential Field

The integration of object detection with artificial potential fields (APF) has recently become a key advancement in path planning for SRL, addressing challenges like local minima and target inaccessibility. Yuan *et al.* enhanced APF for UR5 mechanical arm planning with a novel node selection method to overcome these issues [38], while Yingqi *et al.* successfully integrated the rapidly exploring random tree star (RRT*) with APF, proving its effectiveness in constrained spaces [39]. Luo *et al.* presented work on a six-degree-of-freedom (DOF) serial harvesting robot combining energy optimization with APF for collision-free navigation in dynamic environments [40]. Muhammad *et al.* applied APF in differential drive robots for enhanced maneuverability in dynamic settings [42]. Jiangs team improved APF for obstacle avoidance in a 5-DOF bending robot [43], complemented by the integration of a perturbation observer-based detection with APF for navigating unstructured environments by Salman *et al.* [44].

These pioneering studies have proven successful in their respective domains, primarily focusing on standalone applications or traditional SRL. However, the direct application to the relatively nascent field of SRL presents unique challenges, given the lack of established methods and theories specific to SRL. Nonetheless, these developments offer valuable insights for addressing issues within the SRL domain, providing a reference point for our research. In our work with the SRL platform, we aim to draw upon these integrative techniques, adapting and refining them to fit the specific demands and dynamic nature of SRL operations. The potential of these methods, as demonstrated in previous studies, lays a robust foundation for innovative applications in SRL, promising to enhance their functionality and adaptability in diverse real-world scenarios.

C. Balance Control Strategies for SRL

In the landscape of human-robot collaboration, the challenge of maintaining balance during interaction tasks has prompted innovative control strategies across diverse platforms. Kim *et al.* developed a Model Predictive Control (MPC) framework for humanoid robots that enhances balance through the integration of ankle, hip, and stepping strategies [45]. Building upon the foundation laid by predictive control, Li *et al.* introduced a combination of modified model predictive and impedance control that effectively minimizes disturbances induced by human interaction during object manipulation tasks [46]. Extending the concept of dynamic collaboration, Amirshirzad *et al.* showed that shared control between humans and adaptive robots enhances task performance and speeds learning in ball balancing tasks [47]. However, these methods struggle to dynamically adapt to the variable nature of human movements and the precise demands of SRL in balance tasks, underscoring the need for control strategies that are responsive, predictive, and seamlessly integrated with human biomechanics.

Addressing these limitations, research in SRL for balance control offers a fresh perspective. Luo *et al.* introduced a QR decomposition-based balance controller for SRL, enhancing safety and operational stability in overhead tasks [48]. Tu *et al.* furthered the field with a finite state machine and admittance control for dynamic SRL task transitions, proving the concept with prototype tests [49]. Gonzalez *et al.* innovated with a hybrid control architecture for SRL, improving human-robot balance in transition tasks, tested in nuclear decommissioning scenarios [50]. Despite these advancements, existing strategies primarily enhance task performance or augment human movement without addressing the dynamic collaborative balance required for tasks involving direct interaction between the SRL and human operators, such as jointly supporting an object. This oversight underscores the challenge of integrating SRL into activities needing real-time, adaptive cooperation to maintain the balance and coordination of a shared load. The reliance on predefined kinematic models fails to accommodate the unpredictable variability of human motion, highlighting the necessity for more adaptable, predictive control strategies.

III. METHODOLOGY

The methodology unfolds in three stages to enhance control and precision in SRL operations. The teleoperation strategy begins with IMU-based coarse control for initial maneuvering, progresses to vision-based fine positioning for precise task execution, and concludes with balance control through deformation estimation. Subsequent sections will detail the process, starting with IMU-based teleoperation.

A. IMU-Based Coarse Teleoperation

In SRL teleoperation, the integration of the EKF with IMU emerges as a robust solution for precise state estimation, a process underpinned by the EKF's adeptness at fusing noisy IMU sensor data to refine the SRL's position and orientation in real-time [51], [52]. This strategic combination is essential for teleoperation where accuracy and immediate responsiveness

are paramount. IMU, with their accelerometers and gyroscopes, encounter inherent measurement noise and biases that can cause drift over time. The EKF, specifically designed for nonlinear systems, effectively minimizes the squared error between estimated and actual states through iterative updates, ensuring enhanced state estimation critical for the nuanced demands of SRL teleoperation [53].

For the SRL teleoperation, the state vector x_k is composed of the end-effector's position, velocity, and quaternion orientation:

$$x_k = \begin{bmatrix} p_k, v_k, q_k \end{bmatrix} \quad (1)$$

This vector's evolution is dictated by the system model, accounting for dynamics influenced by acceleration, gravitational forces, and quaternion-based orientation updates:

$$\begin{aligned} p_k &= p_{k-1} + v_{k-1} \cdot dt + 0.5 \cdot (a_{k-1} - g) \cdot dt^2 \\ v_k &= v_{k-1} + (a_{k-1} - g) \cdot dt \\ q_k &= q_{k-1} \otimes q(\omega_{k-1} \cdot dt) \end{aligned} \quad (2)$$

where p_k and v_k correspond to the position and velocity of the end-effector at time k, while q_k indicates its quaternion orientation. The term dt denotes the elapsed time between consecutive estimates, a_{k-1} is the prior step's acceleration, and g signifies constant gravitational acceleration. Angular velocity at the previous step is represented by ω_{k-1}, and quaternion multiplication, denoted by $\otimes$, updates the orientation based on this angular velocity.

The state estimate and covariance matrix are updated as follows:

$$\begin{aligned} G_k &= \mathbf{S}_{k|k-1} \mathbf{F}_k^T \left(\mathbf{F}_k \mathbf{S}_{k|k-1} \mathbf{F}_k^T + \mathbf{Q}_k \right)^{-1} \\ \hat{x}_{k|k} &= \hat{x}_{k|k-1} + G_k \left(z_k - h \left(\hat{x}_{k|k-1} \right) \right) \\ \mathbf{S}_{k|k} &= (I - G_k \mathbf{F_k}) \mathbf{S}_{k|k-1} \end{aligned} \quad (3)$$

Eq. (3) outlines the EKF's update mechanism, where G_k calculating the Kalman gain to assimilate discrepancies between observed and predicted states into the updated estimate. The term $\hat{x}_{k|k}$ represents the adjusted state estimate incorporating this gain, while $S_{k|k}$ signifies the updated covariance matrix, reflecting the certainty of the new estimate. F_k denotes the Jacobian matrix of the state transition function, capturing the dynamics of the system's model relative to the state variables, and Q_k represents the process noise covariance matrix, accounting for the uncertainty in the model dynamics. z_k represents the real-time observation from the Kinect V1 camera, serving as a critical input for correcting the state estimate. $h(\hat{x}_{k|k-1})$ maps predicted states to measurements, allowing for precise adjustment by comparing with actual observations z_k.

A homogeneous transformation 44 matrix $\mathbf{T}$, consisting of a rotation 33 matrix $\mathbf{R}$ and a translation vector $\mathbf{t}$, is used to translate the state vector x_k from the IMU coordinate frame to the SRL's end-effector frame.

$$\mathbf{T} = \begin{bmatrix} \mathbf{R} & \mathbf{t} \\ 0 & 1 \end{bmatrix} \quad (4)$$

To achieve this, the position p_k is extended to homogeneous coordinates p_{hk}, transformed via $\mathbf{T}$ to obtain $p'_{hk} = \mathbf{T} p_{hk}$, and then reverted to standard coordinates as p'_k. Similarly, the orientation q_k is transformed using $\mathbf{R}$, the rotation component of $\mathbf{T}$, to yield a new orientation q'_k, and the velocity v_k is adapted to the end-effector frame as $v'_k = \mathbf{R} v_k$, effectively facilitating the conversion of position, orientation, and velocity to align with the SRL's end-effector frame dynamics.

Through these transformations, the updated state vector is achieved as $x'_k = [p'_k, v'_k, q'_k]$ in the end-effector frame. This facilitates the streamlining of further control or processing tasks within the robotic system.

B. Vision-Enhanced Fine Positioning

Integrating IMU-based coarse teleoperation with vision-based fine control, the system described herein employs a dual-stage control mechanism to guide the end-effector efficiently to its target. Initially, the IMU sensors facilitate rapid, broad movements for preliminary positioning within the target area. Subsequently, the control paradigm seamlessly transitions to a vision-based mode, utilizing high-resolution imagery from a Kinect V1 sensor for detailed object detection, depth information retrieval, and precision manipulation. This approach not only enhances the accuracy of the end-effector in varied task environments but also capitalizes on the strengths of both sensor modalities to ensure adaptive and precise control throughout the operation phases, as depicted in Fig. 2.

1) Target State Detection and Estimation: Object detection utilizes the YOLOX [54] algorithm, generating bounding boxes $B_i = (x_{c,i}, y_{c,i}, w_i, h_i, C_i, L_i)$ for each detected object. These bounding boxes contain the center coordinates $x_{c,i}, y_{c,i}$, dimensions w_i, h_i, confidence score C_i, and class label L_i.

Depth information from the Kinect V1 is then used to calculate the average depth D_i within each bounding box, essential for determining the object's 3D position:

$$D_i = \frac{1}{w_i h_i} \sum_{i=x_{c,i}}^{x_{c,i}+w_i} \sum_{j=y_{c,i}}^{y_{c,i}+h_i} D(i,j) \quad (5)$$

Subsequently, the 3D coordinates P_i in the camera frame are determined using the camera's intrinsic parameters and the computed depth:

$$P_i = \left(\frac{D_i \cdot (x_{c,i} - c_x)}{f_x}, \frac{D_i \cdot (y_{c,i} - c_y)}{f_y}, D_i \right) \quad (6)$$

where f_x and f_y are the camera's focal lengths along the x and y axes, respectively, and c_x and c_y are the coordinates of the principal point in the camera's image sensor.

Finally, the transformation of these coordinates into the world frame is achieved by applying the homogeneous transformation matrix $\mathbf{T}$, which yields the world coordinates (X, Y, Z) of the object as $P_{\text{world}} = \mathbf{T} \cdot [P_i, \quad 1]^{\mathbf{T}}$, seamlessly converting the local coordinates to a global context.

The fine control of the SRL is a critical aspect of achieving precise alignment and manipulation. In this section, we propose an integrated approach that combines the Artificial Potential Field (APF) method with the Tangential Artificial Potential Field (T-APF) method. This approach takes into
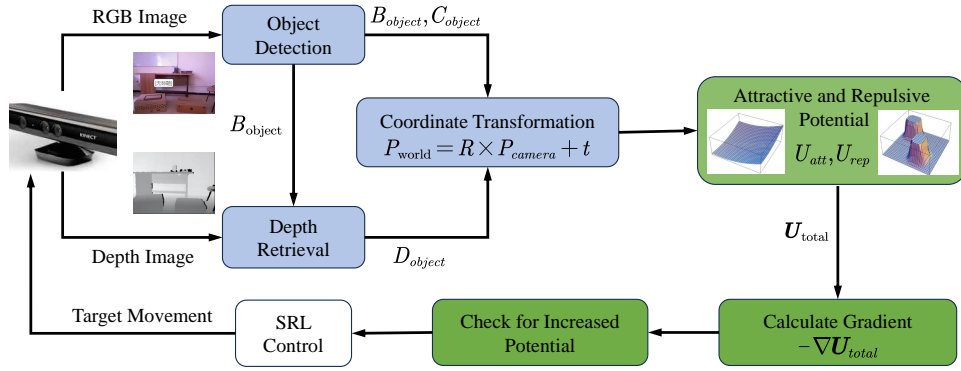
Fig. 2: Integrating perception with T-APF for SRL path planning and navigation

consideration not only the position and velocity information but also directional factors, obstacle velocity, and tangential velocity.

Tangential Artificial Potential Field Model: The Vision-based Artificial Potential Field (VAPF) method models the environment as a field of forces, exerting attractive forces towards the goal and repulsive forces away from obstacles. The T-APF method extends this concept by incorporating tangential components to mitigate the limitations posed by local minima in VAPF models.

The attractive potential field is defined as a quadratic function of the distance to the goal, ensuring that the force decreases as the robot approaches its target. It is mathematically represented as:

$$U_{\text{att}}(q) = \frac{1}{2} k_{\text{att}} \|q - q_{\text{goal}}\|^2 \qquad (7)$$

where q is the position vector of the robot's end-effector, q_{goal} is the position vector of the target, and k_{att} is a positive scaling constant.

The repulsive potential field, in the presence of an obstacle, is traditionally calculated based on the distance to the nearest point on the obstacle surface. For the T-APF, this field is enhanced by including a tangential component, which becomes active in scenarios where traditional methods fail due to local minima. The repulsive potential field is defined as a piecewise function:

$$U_{\text{rep}}(q) = \begin{cases} \frac{1}{2} k_{\text{rep}} \left(\frac{1}{\|q - q_{\text{obs}}\|} - \frac{1}{\rho_0} \right)^2, & \text{if } \|q - q_{\text{obs}}\| \leq \rho_0 \\ & \text{and } \mathbf{n}_{\text{obs}} \cdot \mathbf{t}_{\text{obs}} = 0 \\ k_{\text{tan}} \left(\frac{1}{\|q - q_{\text{obs}}\|} - \frac{1}{\rho_0} \right) \mathbf{t}_{\text{obs}}, & \text{if } \|q - q_{\text{obs}}\| \leq \rho_0 \\ & \text{and } \mathbf{n}_{\text{obs}} \cdot \mathbf{t}_{\text{obs}} \neq 0 \\ 0, & \text{otherwise} \end{cases}$$
$$(8)$$

where q_{obs} denotes the position vector of the closest point on the obstacle, $\mathbf{n}_{\text{obs}}$ is the normal vector at the closest point, $\mathbf{t}_{\text{obs}}$ is the tangential unit vector along the obstacle edge, k_{rep} and k_{tan} are positive constants representing the strengths of the repulsive and tangential forces, respectively, and ρ_0 is the influence range of the obstacle. Considering non-orthogonal $\mathbf{n}_{\text{obs}}$ and $\mathbf{t}_{\text{obs}}$ accommodates irregular surface features and strategic navigation adjustments, enhancing flexibility in com-

---

Algorithm 1 FSM-based Planning Model with T-APF

$U_{\text{att}}(q) = \frac{1}{2} k_{\text{att}} \|q - q_{\text{goal}}\|^2$
while not at q_{goal} **do**
    Initialize position adjustment $\Delta q(q) \leftarrow 0$
    for each obstacle o in O **do**
        $d \leftarrow \|q - q_{\text{obs}}\|$
        if $L_o \in O_{\text{plane}}$ and $d \leq \rho_{\text{plane}}$ **then**
            $\mathbf{n}_{\text{obs}} \leftarrow \text{GetNormalVector}(P_o, w_o, h_o)$
            $\mathbf{t}_{\text{obs}} \leftarrow \text{GetTangentVector}(P_o, \mathbf{n}_{\text{obs}})$
            $U_{\text{rep}}(q, o) \leftarrow \frac{1}{2} k_{\text{plane}} \left(\frac{1}{d} - \frac{1}{\rho_{\text{plane}}} \right)^2$
        else if $L_o \in O_{\text{sphere}}$ and $d \leq \rho_{\text{sphere}}$ **then**
            $\mathbf{n}_{\text{obs}} \leftarrow \frac{q - P_o}{\|q - P_o\|}$
            $\mathbf{r} \leftarrow \text{RandomNonParallelVector}(\mathbf{n}_{\text{obs}})$
            $\mathbf{t}_{\text{obs}} \leftarrow \frac{\mathbf{n}_{\text{obs}} \times \mathbf{r}}{\|\mathbf{n}_{\text{obs}} \times \mathbf{r}\|}$
            $U_{\text{rep}}(q, o) \leftarrow \frac{1}{2} k_{\text{sphere}} \left(\frac{1}{d} - \frac{1}{\rho_{\text{sphere}}} \right)^2$
        end if
        if $d \leq \rho_0$ and $\mathbf{n}_{\text{obs}} \cdot \mathbf{t}_{\text{obs}} \neq 0$ **then**
            $U_{\text{rep}}(q, o) \leftarrow k_{\text{tan}} \left(\frac{1}{d} - \frac{1}{\rho_0} \right) \mathbf{t}_{\text{obs}}$
        else
            $U_{\text{rep}}(q, o) \leftarrow 0$
        end if
        $\Delta q(q, o) \leftarrow -\nabla U_{\text{rep}}(q, o)$
        $\Delta q(q) \leftarrow \Delta q(q) + \Delta q(q, o)$
    end for
    Compute total adjustment $\Delta q(q) \leftarrow \Delta q(q) - \nabla U_{\text{att}}(q)$
    Update position $q \leftarrow q + \Delta q(q)$
end while

---

plex environments. Finally, the total potential field is expressed as $\boldsymbol{U}_{\text{total}} = U_{\text{rep}}(q) + U_{\text{att}}(q)$.

In Algorithm 1, a finite state machine (FSM) is employed to categorize and manage different types of obstacles. For planar obstacles, the model calculates normal and tangent vectors using geometric methods. The `GetNormalVector` computes the normal vector using three non-collinear points, which defines the perpendicular direction to the obstacle surface based on its width w_o, height h_o, and central position P_o. The `GetTangentVector` computes the tangent vector, crucial for enabling sliding motions along obstacles and freeing the robot from local minima caused by the equilibrium of forces on flat surfaces. For spherical obstacles, it simplifies the process to accommodate their standard spherical characteristics. The `RandomNonParallelVector` generates a random vector that is not parallel to the normal vector $\mathbf{n}_{\text{obs}}$,

ensuring that the computed tangent vector can effectively guide the robot around the curved surfaces of spherical obstacles.

By incorporating tangential and normal components into repulsive potentials, the T-APF method enhances interaction with obstacles by enabling tangential navigation and minimizing the risk of encountering local minima. This approach reduces the likelihood of the system encountering local minimaa common limitation in traditional potential field methodsthereby enhancing the safe and efficient path planning capabilities of SRL. However, to achieve harmonious, synchronized interaction between the operator and the SRL, anticipating the operator's movements is crucial, especially in dynamic environments where intentions can change rapidly.

C. Balance Control Based on Deformation Estimation

In this section, the methodology employed for balance control in SRL operations is elaborated upon. The process involves translating real-time feedback from the SRL's end-effector's pose into meaningful deformation estimates. These estimates are then utilized to predict and adjust the SRL's movements, ensuring effective balance support, even when the hand is in motion.

Fig. 3 illustrates the estimation of deformation using the Dual-Spring model and the prediction of motion in the SRL. This framework intricately combines deformation estimation with human motion prediction, leveraging the dual-spring model to analyze and quantify both translational and rotational deformations resulting from pose changes. Fig. 4 illustrates the control methodology for the SRL, integrating the principles of variable impedance control with a dual-spring model. This framework is designed to leverage the predicted movements of the hand, facilitating a dynamic and responsive control mechanism. By employing the dual-spring model, the framework adeptly simulates and responds to both translational and rotational forces, ensuring a balanced interaction between the SRL and the operator.

Deformation Estimation from Pose Data: The pose of the SRL's end-effector is represented in the Special Euclidean Group $\mathrm{SE}(3)$, encapsulating both translational and rotational components. Real-time changes in the pose are captured and translated into deformation estimates, which are crucial for dynamic control.

The pose $\mathbf{M}$ of the end-effector and its change between two instances can be efficiently represented by a homogeneous transformation matrix and its differential change, respectively:

$$\mathbf{M} = \begin{bmatrix} \mathbf{R} & \mathbf{p} \\ 0 & 1 \end{bmatrix}, \quad \Delta\mathbf{M} = \mathbf{M}_2\mathbf{M}_1^{-1} = \begin{bmatrix} \Delta\mathbf{R} & \Delta\mathbf{p} \\ 0 & 1 \end{bmatrix} \quad (9)$$

where $\mathbf{R} \in \mathrm{SO}(3)$ is the rotation matrix, $\mathbf{p}$ is the translation vector specifying the end-effector's position, $\Delta\mathbf{R}$ captures the rotational change, and $\Delta\mathbf{p}$ the translational change, succinctly combining both aspects of movement within the $\mathrm{SE}(3)$ space.

The transformation of the pose change $\Delta\mathbf{M}$ to the corresponding Lie algebra SE(3) provides a compact and efficient representation of the end-effector's motion. Through a logarithmic map, $\Delta\mathbf{M}$ is converted into a rotational and linear velocity vectors in the Lie algebra [55]:

$$\begin{bmatrix} \boldsymbol{\omega} \\ \boldsymbol{v} \end{bmatrix} = \mathrm{Log}\left(\Delta\mathbf{M}\right) \quad (10)$$

where $\boldsymbol{\omega}$ and $\boldsymbol{v}$ correspond to the rotational and translational velocities, respectively. These velocity components are crucial for dynamically adjusting the Hook's law constants K_{trans} and K_{rot} in the dual-spring model.

To facilitate smoother interactions, the spring model's stiffness is dynamically adjusted in real-time, responsive to the deformation velocity. Assuming logarithmic relationships between the velocity components and the spring constants, the dynamic adjustment of K_{trans} and K_{rot} is adjusted as follows:

$$\begin{aligned} K_{\mathrm{trans}} &= \gamma_{\mathrm{trans}} \log\left(1 + |\boldsymbol{v}|\right) \\ K_{\mathrm{rot}} &= \gamma_{\mathrm{rot}} \log\left(1 + |\boldsymbol{\omega}|\right) \end{aligned} \quad (11)$$

where the scaling factors γ_{trans} and γ_{rot} dynamically modulate the stiffness of K_{trans} and K_{rot} based on translational and rotational velocities, respectively. The logarithmic scaling ensures that the spring constants respond smoothly to velocity changes, increasing sensitivity and responsiveness at lower speeds and providing greater stability and robustness at higher velocities, which is essential for balance tasks. Notably, the logarithmic function $\log()$ applied here specifically adjusts spring constants for velocity responsiveness and is conceptually distinct from the Lie algebra's $\mathrm{Log}()$.

Translational deformation is approximated as $\boldsymbol{p} = \Delta\mathbf{p}$. For rotational deformation, understanding and quantifying it requires decomposing the rotation matrix $\Delta\mathbf{R}$ into its constituent elementsrotation angle θ and rotational axis $\boldsymbol{u}$.

The rotation angle θ is derived from the trace of the rotation matrix $\Delta\mathbf{R}$:

$$\theta = \arccos\left(\frac{\mathrm{tr}(\Delta\mathbf{R}) - 1}{2}\right) \quad (12)$$

where $\mathrm{tr}(\Delta\mathbf{R})$ denotes the trace of $\Delta\mathbf{R}$, representing the sum of its diagonal elements. This formulation is based on the properties of rotation matrices within the special orthogonal group SO(3).

Following the determination of θ, the rotational axis $\boldsymbol{u}$ is computed from the skew-symmetric part of $\Delta\mathbf{R}$:

$$\boldsymbol{u} = \frac{1}{2\sin(\theta)} \begin{bmatrix} \Delta\mathbf{R}_{32} - \Delta\mathbf{R}_{23} \\ \Delta\mathbf{R}_{13} - \Delta\mathbf{R}_{31} \\ \Delta\mathbf{R}_{21} - \Delta\mathbf{R}_{12} \end{bmatrix} \quad (13)$$

This approach extracts $\boldsymbol{u}$ by utilizing the properties of skew-symmetric matrices, where the elements of $\Delta\mathbf{R}$ outside the main diagonal are instrumental.

With θ and $\boldsymbol{u}$ established, the Rodrigues' rotation formula can be applied to reconstruct or validate the rotation matrix $\mathbf{R}$. The skew-symmetric matrix $\mathbf{K}$ formed from $\boldsymbol{u}$ is:

$$\mathbf{K} = \begin{bmatrix} 0 & -u_z & u_y \\ u_z & 0 & -u_x \\ -u_y & u_x & 0 \end{bmatrix} \quad (14)$$

Using $\mathbf{K}$, the Rodrigues' rotation formula is expressed as:

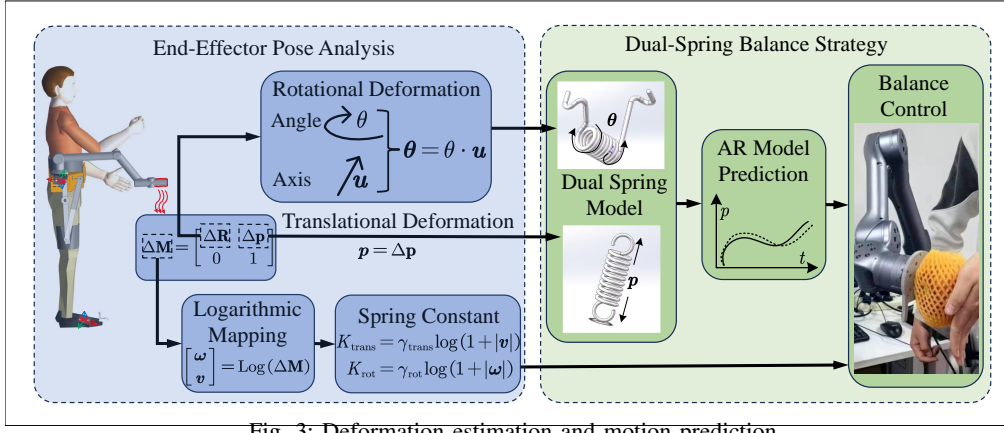$$\mathbf{R} = \mathbf{I} + (\sin\theta)\mathbf{K} + (1 - \cos\theta)\mathbf{K}^2 \quad (15)$$

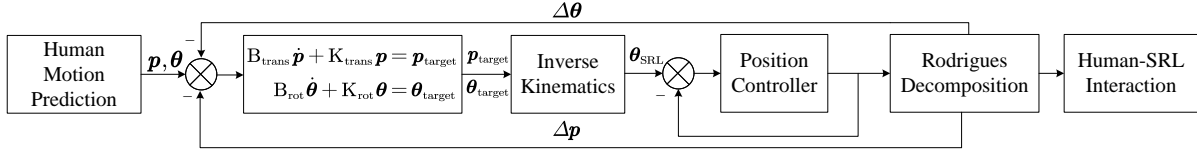Fig. 3: Deformation estimation and motion prediction

Fig. 4: The diagram of the proposed balance control strategy.

where $\mathbf{I}$ is the identity matrix. This formula provides a method to convert the rotation vector, characterized by θ and yellow $\boldsymbol{u}$, into a rotation matrix.

The rotational deformation vector yellow $\boldsymbol{\theta}$, which represents the rotational change in the end-effector's pose, is computed as $\boldsymbol{\theta} = \theta \cdot \boldsymbol{u}$, where θ is the rotation angle and $\boldsymbol{u}$ is the rotation axis. The rotation matrix $\mathbf{R}$, derived from $\boldsymbol{\theta}$ using Rodrigues' rotation formula, is then utilized to adjust the orientation of the end-effector's vectors accordingly.

After estimating the deformation vectors $\boldsymbol{p}$ and $\boldsymbol{\theta}$, it is crucial to adjust these estimates to accurately reflect the hand's real-world position and orientation, ensuring the SRL and hand maintain their requisite spatial relationship for synchronized movement and task execution.

The position and orientation of the hand, denoted by m_{human}, are determined through the formula:

$$m_{\text{human}} = \alpha\boldsymbol{p} + \beta\mathbf{R}\left(\boldsymbol{\theta}\right) \cdot \boldsymbol{t}_{\text{offset}} \tag{16}$$

where $\mathbf{R}\left(\boldsymbol{\theta}\right)$ denotes the rotation matrix calculated from the rotational deformation vector $\boldsymbol{\theta}$, which adjusts the offset vector $\boldsymbol{t}_{\text{offset}}$ to align with the current orientation of the SRL's end-effector. The coefficients α and β are scaling factors that adjust the contribution of positional and orientational components, respectively, ensuring m_{human} accurately reflects the hand's position and orientation in relation to the SRL's end-effector.

Then m_{human} is fed into the AR predictive model. The AR model utilizes the current and historical data of the deformation estimates to forecast the future position and orientation of the SRL's end-effector.

To elevate the synchronization between the human and the SRL, we harness the predictive power of the AR model, which has been demonstrated to effectively predict human motion in interactive robotic applications [15]. An AR model of order $\boldsymbol{p}$

is employed to forecast the human arm's trajectory:

$$m_{\text{pred}}\left(t\right) = c + \sum_{i=1}^{p} \phi_i m_{\text{human}}\left(t - i\right) + \epsilon_t \tag{17}$$

where $\mathbf{x}_{\text{pred}}(t)$ denotes the predicted motion at time t, c is a constant term, ϕ_i are the AR coefficients, and ϵ_t represents the error term. The parameters c, ϕ_i, and ϵ_t are estimated using statistical techniques that fit the AR model to historical data of human motion. Specifically, the least squares method is employed to optimize these parameters, ensuring that the predicted trajectory $\mathbf{x}_{\text{pred}}(t)$ closely matches the observed movements, thus minimizing the error term ϵ_t.

The AR coefficients ϕ_i are estimated using the method of least squares. The update law for the coefficients is given by:

$$\phi = \left(\mathbf{X}^T\mathbf{X}\right)^{-1}\mathbf{X}^T\mathbf{y} \tag{18}$$

where $\mathbf{X}$ is the matrix of lagged observations, and $\mathbf{y}$ is the vector of observations.

Closed-Loop Control for SRL: Based on the predicted motion obtained from the AR model, a closed-loop strategy is implemented to control the SRL, by integrating a dual-spring model controller with numerical inverse kinematics.

The control process begins with the dual-spring model controller, which takes the estimated translational and rotational deformations as inputs. These deformations, denoted as $\mathbf{p}$ and $\boldsymbol{\theta}$, are derived from the real-time pose data of the SRL's end-effector. The controller then computes the desired end-effector position and orientation using the following equations:

$$\begin{aligned}\mathbf{B}_{\text{trans}}\dot{\boldsymbol{p}} + \mathbf{K}_{\text{trans}}\boldsymbol{p} = \boldsymbol{p}_{\text{target}}\\ \mathbf{B}_{\text{rot}}\dot{\boldsymbol{\theta}} + \mathbf{K}_{\text{rot}}\boldsymbol{\theta} = \boldsymbol{\theta}_{\text{target}}\end{aligned} \tag{19}$$

where $\mathbf{B}_{\text{trans}}$ and $\mathbf{B}_{\text{rot}}$ are the damping matrices for translational and rotational movements, respectively, while $\mathbf{K}_{\text{trans}}$ and $\mathbf{K}_{\text{rot}}$ represent the stiffness matrices. The target positions, $\boldsymbol{p}_{\text{target}}$ and

θ_{target}, are the outputs of the controller that guide the SRL towards the desired pose.

It is noted that human tremor brings high-frequency noise into p and θ [56]. This noise potentially affects the accuracy of the deformation inputs to the control system. The control system described by Eq. (19) effectively mitigates these disturbances through its structural components. Specifically, the damping matrices B_{trans} and B_{rot}, along with the differential components $\dot{p}$ and $\dot{\theta}$, function analogously to a low-pass filter. This filtration mitigates the impact of low-frequency noise by dampening its influence before it can affect the control outputs. Hence, the system maintains robustness against the kind of noise predominantly introduced by human tremors, ensuring the accuracy and stability of the SRLs movements towards the target positions p_{target} θ_{target}.

This methodology is anchored on a closed-loop control system that is integral to the precision and adaptability in SRL operations. Initially, the system employs inverse kinematics to convert the target pose into specific SRL joint angles, crucial for achieving the desired position. Following the execution of movement, the system engages in a feedback loop where the SRL's end-effector pose is re-evaluated. This updated information, combined with data from the AR predictive model, informs new deformation estimates, which are then fed back into the dual-spring model controller.

IV. Experiment and Results

A. Experiment Setup

In designing the six degrees of freedom SRL mounted on the right side of the human body, safety was paramount. The SRL's base is strategically positioned at the waist on the right side to optimize movement range and comfort while minimizing unwanted contact with the user's front and left sides. Advanced safety features integrated into the system include joint force feedback and collision detection mechanisms, which actively monitor interactions and adjust or halt movements if necessary. Additionally, operators are equipped with safety goggles and helmets to enhance safety during operations.

As shown in Fig. 1 and Fig. 5, two IMU sensors play a pivotal role in this setup. The first IMU sensor is ingeniously affixed to the dorsum of the foot. To ensure stability and reliability, the first IMU is attached using a specially designed connector that snugly clips onto the shoe, ensuring minimal movement and optimal data accuracy. The second IMU is mounted at the base of the SRL, functioning as a vital element for the real-time updating of the SRL's base pose, which in turn refines the end-effector's position. This setup facilitates the operator's left hand in supporting the object while the right hand is engaged in other tasks or holding another object. For vision-based control, a Kinect V1 camera is positioned on a nearby table, calibrated to have a clear field of view encompassing both the SRL and the object of operation. This placement ensures real-time visual feedback, crucial for precise robotic movements.

The SRL's base is firmly anchored to the operator using a specially designed harness, ensuring stability during operations. The entire prototype, including the SRL and the sensing system, weighs approximately 5 Kg. A 3D-printed end-effector is integrated into the SRL, designed to ensure effective and stable interactions with a variety of objects.

The software system for the SRL operates on a desktop computer running Ubuntu 20.04, equipped with a GTX 3060 GPU and configured with the CUDA environment. The Robot Operating System (ROS) serves as the interface between the SRL and the sensing system, managing the controller codes and ensuring seamless integration and operation.

Two male subjects with varying physical attributes (Subject 1: height 180 cm, weight 73 Kg; Subject 2: height 175 cm, weight 70 Kg) were recruited to participate in the experiment. Before the main experiment, participants were briefed about the task and the collaboration mechanism between the human and the SRL. A preliminary session was conducted to familiarize the participants with the SRL system, where they wore the prototype to adjust to its weight and collaborated with the SRL multiple times to understand the task. The subjects collaborated with the SRL to balance and move an object (e.g., a sphere or a cube) in free space without letting it fall. The success of the task was determined by the stability and duration for which the object remained balanced and airborne.

B. IMU-Based Coarse Teleoperation Experiment

In the experiment depicted in Fig. 5, the SRL's precision and responsiveness to IMU control were evaluated. These tests involved guiding the SRL to follow predetermined trajectories and orientations based on operator-generated IMU data, focusing on the system's ability to translate these inputs into accurate and stable end-effector movements. Fig. 6 further visualizes and quantitatively analyzes a specific teleoperation trajectory, comparing the SRL's actual position to the control inputs, thus enabling a detailed assessment of the system's performance and accuracy in replicating human-intended paths.

Quantitative Error Assessment: The position errors were quantitatively analyzed by calculating the Euclidean distance between corresponding points on the actual position and control input trajectories throughout the experiment. The mean positional error was 0.553 mm, indicating the average deviation. Furthermore, when considering the standard deviation, the upper bound of error (mean + STD) was found to be 1.553 mm. Such a level of accuracy is often considered acceptable for a wide range of teleoperated tasks. The inclusion of standard deviation in this analysis also provides insight into the variability of the system's performance, further affirming the reliability of the IMU-based approach in replicating human-intended trajectories.

Temporal Analysis of Errors: During the experiment, a notable observation was the emergence of peaks in the moving average of positional errors, specifically between 1.3 seconds and 2.5 seconds. These peaks indicated significant deviations between the original and smoothed trajectories of the SRL's end-effector. A critical factor contributing to these error peaks was identified as the sudden changes in the movement direction of the SRL. Such abrupt directional shifts introduce inertia, which in turn causes compensatory human body movements. This result may lead to a reduction in control precision,
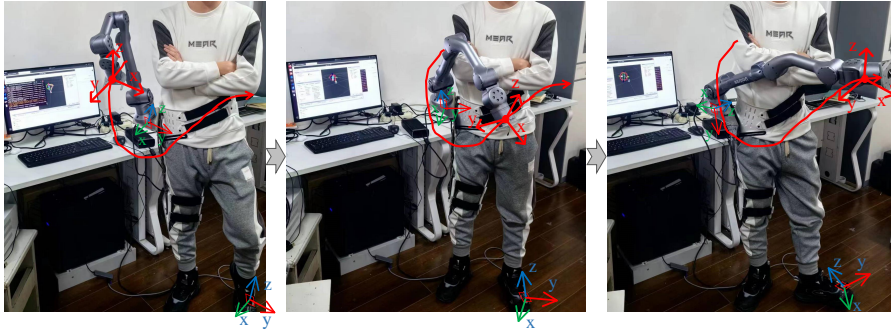
Fig. 5: Screenshots of the IMU-Based teleoperation experiment.
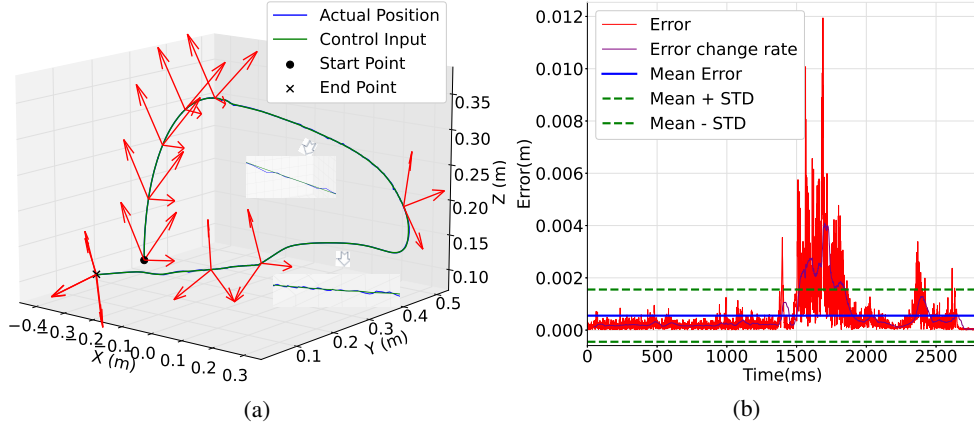

(a) (b)

Fig. 6: (a) displays the SRL's actual position versus desired trajectories during IMU-Based teleoperation. It arrows on trajectories indicate orientation control, showcasing precise orientation adjustments alongside positional tracking. (b) illustrates positional discrepancies between actual and desired trajectories, providing insights into the IMU-Based system's accuracy.

especially in a system where human movements directly influence the teleoperation of robotic limbs. In instances of rapid directional changes, the inertia generated by the SRL can impact the operator's stability and control precision. This interaction is a potential reason for the observed peaks in position errors.

C. Vision-Enhanced Fine Positioning Experiment

In this experiment, the initial phase involved using IMU-based control to bring the target within the camera's field of view, a prerequisite for the subsequent phase of the experiment. Once the target was visually acquired, the focus shifted to a vision-based servo control mechanism, which was employed to guide the SRL's end-effector with greater precision to its intended location. To enhance the precision and effectiveness of the T-APF used in guiding the SRL, parameters were selected based on optimization trials that aimed to minimize potential conflicts and ensure smooth navigation around obstacles. The attraction constant k_{att} was set at 0.84, while the repulsive constants for planar and spherical obstacles were determined as $k_{plane} = 6.25$ and $k_{sphere} = 4.14$, respectively, with an influence range ρ_0 of 4 cm to effectively balance attraction and repulsion forces within the systems operational environment.

Comparative Performance Analysis: A comparison of trajectories generated by the VPF and T-APF methods within a multi-obstacle setting, as shown in Fig. 7(a), reveals the

T-APF's notably smoother path, minimizing detours and reducing travel time. Smoothness analysis, detailed in Fig. 7(b), underscores the T-APF method's efficiency with a significantly higher mean velocity, indicating a more direct approach to the destination. The stability and consistency of the T-APF's obstacle avoidance strategy, evident in its line graph, ensure smooth movements essential in cluttered environments. This smoother navigation, characterized by reduced erratic accelerations, is crucial for the comfort and safety of wearable robotic systems like SRL. The T-APF method's adeptness at maintaining steady movements while effectively navigating around obstacles demonstrates its suitability for SRL platforms, highlighting its potential to enhance wearable robotics.

The comparative analysis of repulsive forces between the T-APF and VPF methods, illustrated in Fig. 7(c), revealed distinct behavioral patterns, with both methods experiencing an increase in repulsive force as obstacles approached the target. However, the T-APF method exhibited a more consistent and controlled repulsive force profile, indicating a more balanced approach to obstacle avoidance. Unlike VPF, T-APF maintained generally lower repulsive forces, even in scenarios with closer obstacles, suggesting its nuanced operation that enhances smoother human-robot integration and minimizes abrupt movements. This lower repulsive force magnitude, alongside efficient obstacle navigation, highlights T-APF's superiority in ensuring safety and comfort for the operator.
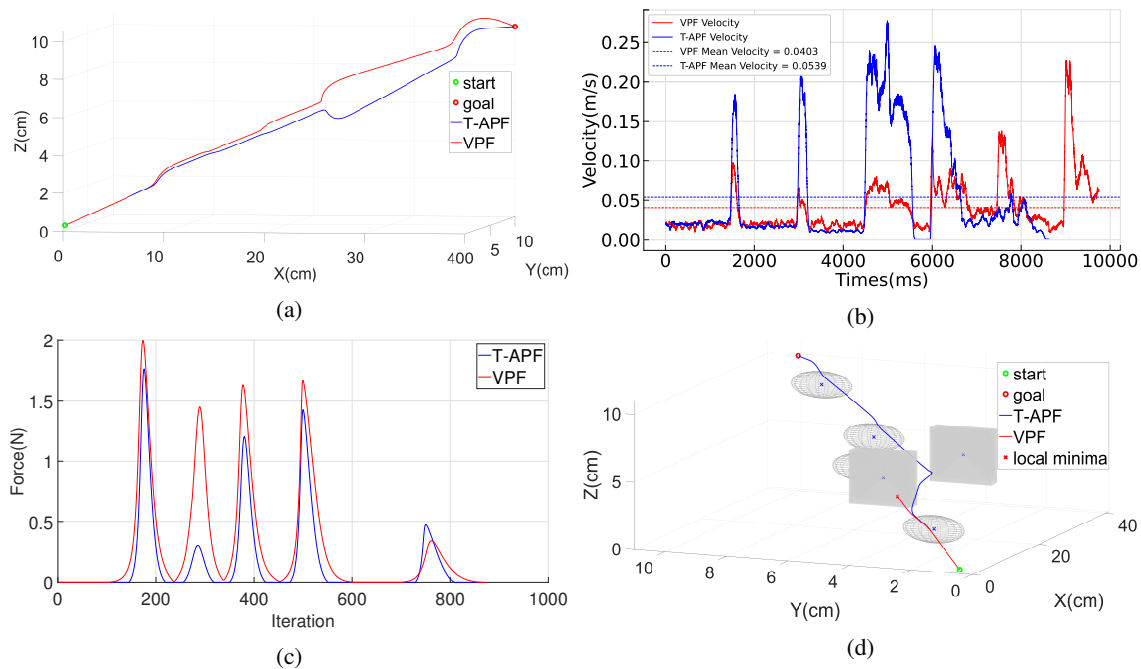
Fig. 7: (a) displays paths by VPF and T-APF methods, visually comparing their trajectories and obstacle avoidance efficiency. (b) shows the impact of each iteration on path smoothness. (c) compares the differences in repulsive forces over time for VPF and VPF methods, indicating their responses to obstacles and avoidance strategies. (d) dispalys scenarios with large plane obstacles, comparing T-APF and VPF methods' effectiveness in escaping local minima caused by the force counteraction.

Performance Metrics: The experimental series was designed to assess the resilience and adaptability of the T-APF and VPF methods within simulated SRL system scenarios, mirroring potential real-world applications by varying obstacle configurations while maintaining constant start and end points. Performance evaluation, as summarized in Table 1, focused on total time, total displacement, and average minimum distance from obstacles, key indicators of efficiency, accuracy, and safety in dynamic path planning.

Results demonstrated the T-APF method's consistent superiority over VPF, particularly in reducing total time, thereby indicating faster navigation through diverse obstacle layouts. Although the T-APF method resulted in slightly higher total displacement, this reflects its dynamic pathfinding approach. Notably, the T-APF method's average minimum distance from obstacles is marginally smaller than that of VPF, showcasing a more deliberate strategy in handling obstacles, which is an essential balance for SRL applications.

The conducted experiments have unequivocally established the T-APF method's superiority in SRL operations, attributable to its enhanced performance in path smoothness, target-reaching efficiency, and obstacle avoidance stability. The T-APF method's ability to achieve targets quickly and with smooth trajectories sets a benchmark in SRL operations, crucial for tasks where time is of the essence. Notably, a higher path smoothness mean value signifies stable and predictable movements, essential for the precise operation of SRL in environments demanding accurate navigation. Furthermore, compared to the VPF method, the T-APF method demonstrates a lower, more controlled repulsive force profile, facilitating smoother integration with human movements and minimizing

the risk of sudden destabilizing actions. This capability of maintaining minimal repulsive forces while adeptly navigating around obstacles underscores the T-APF method's alignment with key SRL operational requirementsbalance, safety, and comfort. These findings underscore the T-APF method's suitability for SRL applications, advancing wearable robotics and enhancing the potential for SRL use in precision-critical real-world scenarios.

TABLE I: Key metrics for the performance comparison

Parameters	T-APF	VPF
Total Time(ms)	8660	9875
Total Displacement(cm)	46.421	44.670
Average Minimum Distance	7.6235	8.2546

D. Balance Experiment with Deformation Estimation and AR Prediction

Building upon the precision attained through vision-enhanced fine positioning, the third phase of the experiment focused on the balance support task using the SRL, as shown in Fig. 8. In this experiment, the SRL's end-effector and the hand cooperatively held an object. The parameters $\gamma_{trans} = 0.812$, $\gamma_{rot} = 0.5044$, $B_{trans} = 1.2\,\text{Ns/m}$, $K_{trans} = 2.5\,\text{N/m}$, $B_{rot} = 0.6\,\text{Ns/rad}$, $\alpha = 0.8869$, $\beta = 1.28$, and $K_{rot} = 1.1\,\text{Nm/rad}$ were empirically tuned and validated against the requirements of the balance task and the dynamics of the system. This selection process ensures an optimal balance between responsiveness and stability across varying velocity ranges.

The extraction of translational and rotational deformation vectors from the positional data of the SRL's end-effector is

key to this experiment. These variables were fed into an AR model for predicting the robot's next actions. The predictions, combined with the accumulated potential energy from the spring model, provided the next predicted pose of the SRL's end-effector, which was then used for control inputs. This methodology ensured that even if the hand moved, the SRL and the object could maintain a dynamic balance within a certain range.

Analysis of Deformation Estimation: The comprehensive analysis conducted on deformation estimation within SRL operations aimed to validate the feasibility and accuracy of the proposed method for deformation extraction. This section presents an in-depth examination of the data from the first set of experiments, encompassing four critical graphs: Fig. 9(a) deformation translations *vs.* control inputs, Fig. 9(b) deformation rotations *vs.* control inputs, Fig. 9(c) translation deformations over time, and Fig. 9(d) rotation deformations over time.

The data presented in Figs. 9(a)- 9(b) demonstrated the accuracy of our dual-spring model for estimating deformation in SRL operations. In Fig. 9(a), the congruence of cumulative translational deformation trends in the X and Y axes with the control inputs underscores the precision of our method. Overall, deformation trends across all axes align with expected trajectories; however, the Z-axis exhibits a consistent 0.17 m deviation due to object handling activities between the hand and the SRL end-effector. Fig. 9(b), depicting cumulative rotational deformations, shows a similar pattern of alignment with control inputs. Notable errors during larger changes suggest the influence of sliding friction between the hand and the object, leading to minor miscalculations in deformation estimates. These observations validate the effectiveness of the dual-spring model in estimating deformations accurately.

Further analysis from Figs. 9(c)-9(d) reinforces the reliability of our method. These graphs display real-time changes in translational and rotational deformations. The overall stability in deformation changes is evident, with minor fluctuations such as the sudden increase in Y-direction translation at approximately 1.6 s (0.024 m unit deformation) and a similar perturbation in the X-axis at 3.1 s. These instances, likely caused by external disturbances, correlate with noticeable jitter in the corresponding curves. Additionally, rotational deformations in the Yaw direction exhibit significant fluctuations at around 1.7 s and 3 s, reaching up to 0.096 rad. These findings highlight the models capacity to maintain steady deformation estimates despite occasional external perturbations.

Analysis of AR Prediction for Balance Control: The exploration of the AR predictive model within SRL operations involved meticulously designed experiments and analyses to evaluate the model's efficacy in enhancing balance and precision in human-robot interaction tasks. The six graphical representationsencompassing 3D deformation translations and rotations in response to control inputs, along with their predictions and respective prediction errorswere not merely illustrative but served a deeper analytical purpose as depicted in Fig. 10.

The experiments involving 3D deformation translations and rotations versus control inputs (Figs. 10(a)-10(b)) aimed to es-

tablish a foundational understanding of how SRL movements correlate with the control inputs, thereby affirming the model's responsiveness and accuracy. The subsequent predictions for translations and rotations (Figs. 10(c)-10(d)) are critical in assessing the AR model's capability to anticipate the future movements of the SRL based on current and historical data, a key aspect in maintaining dynamic balance in collaborative tasks. Furthermore, the analysis of prediction errors for both translations and rotations (Figs. 10(e)-10(f)) provided insights into the precision and reliability of the AR model.

In these experiments, the roles of deformation estimation and AR predictive modeling in enhancing balance support tasks using SRL are rigorously evaluated. The results demonstrate the effectiveness of the deformation estimation method in capturing the intricate interactions of SRL with supported objects, crucial for precise operation in dynamic environments. This method quantifies translational and rotational deformations, enabling real-time adaptation of the SRL's movements to maintain stability and alignment. Furthermore, the incorporation of AR predictive modeling augments SRL operations by forecasting movements, allowing the SRL to adjust its support proactively. This predictive capability facilitates smoother and more compliant human-robot interactions, as evidenced by low prediction errors, thereby enhancing the success rate of balance support tasks. Overall, the data-driven analysis confirms that both deformation estimation and AR predictive modeling are integral to achieving precise and synchronized movements in SRL applications, particularly in tasks requiring close human-robot collaboration.

V. CONCLUSION

In this study, we present a comprehensive control strategy for SRL, integrating IMU-based coarse teleoperation refined by the EKF, a dual-spring model for dynamic balance, and vision-based techniques for enhanced object detection and path planning. The synergy between IMU and EKF facilitates initial coarse movement control, setting a foundation for subsequent tracking. The dual-spring model, essential for mimicking natural limb dynamics, improves the intuitive operation of SRL. Concurrently, vision-based technology refines the system's accuracy in object detection and navigation within complex environments. The proposed control strategy has been experimentally validated on a prototype SRL, showcasing advancements in task execution precision and adaptability, alongside improved human-SRL coordination.

However, we also identified key limitations that impact the systems performance and reliability. The dual-spring model exhibits high sensitivity to parameter tuning, leading to potential deviations under dynamic conditions. Additionally, the EKF struggles with rapid dynamic changes, affecting response times and accuracy. These issues underscore the need for more adaptive algorithms that can manage sudden changes effectively. Moreover, while vision-based positioning performs well in controlled settings, variable environmental factors like lighting changes and physical obstructions compromise its efficacy, particularly in outdoor or unstructured settings.

Future work will focus on integrating machine learning for real-time parameter adjustment to improve the adaptability and
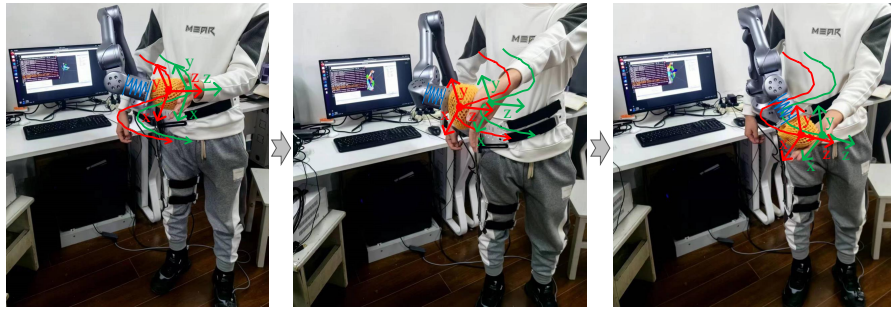
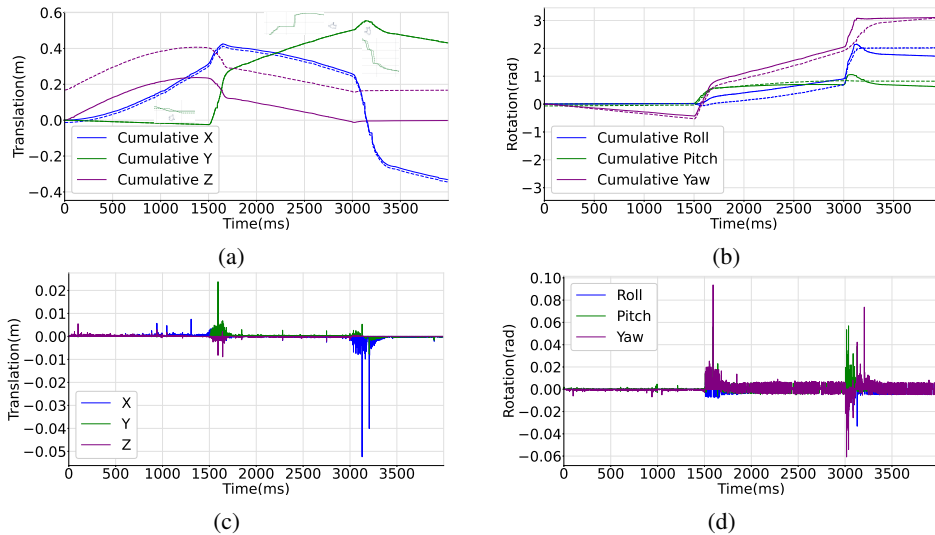Fig. 8: Screenshots of the balance control experiment.

Fig. 9: (a) and (b) depicted the correlation between the control inputs and the deformation translations and rotations, respectively. The control inputs were derived by integrating the changes in the SRL's end-effector position with the support distance (the width of the object).

robustness of SRL systems. This approach will utilize dynamic tuning mechanisms to optimize system parameters continuously based on real-time feedback. Furthermore, expanding the range of sensory inputs to include thermal imaging and LIDAR will address the limitations of vision-based positioning, enabling more reliable and accurate navigation and object detection across various environments. These advancements are expected to refine SRL performance in demanding applications such as disaster response, advanced manufacturing, and medical surgeries, where precision and adaptability are paramount.

REFERENCES

[1] D. Prattichizzo, M. Pozzi, T. L. Baldi, M. Malvezzi, I. Hussain, S. Rossi, G. Salvietti, "Human augmentation by wearable supernumerary robotic limbs: review and perspectives," *Progress in Biomedical Engineering.*, vol. 3, pp. 303–312, 2021.

[2] MA. Sada, T. Hglund, M. Khamis, J. Urbani, T. Nakajima, "Orochi: Investigating Requirements and Expectations for Multipurpose Daily Used Supernumerary Robotic Limbs," *Proceedings of the 10th Augmented Human International Conference.*, vol. 1, pp. 1–9, 2019.

[3] BA. Llorens-Bonilla, "Supernumerary robotic limbs: task planning, execution, and prediction-based coordination with the human wearer," *Massachusetts Institute of Technology.*, 2013.

[4] E. Abdi, E. Burdet, M. Bouri, H. Bleuler, "Control of a Supernumerary Robotic Hand by Foot: An Experimental Study in Virtual Reality," *PloS one.*, vol. 10, pp. 34–42, 2015.

[5] B. Yang; J. Huang; X. Chen; C. Xiong; Y. Hasegawa, "Supernumerary robotic limbs: a review and future outlook," *IEEE Transactions on Medical Robotics and Bionics.*, vol. 3, pp. 623-639, 2021.

[6] I. Hussain, Giovanni Spagnoletti, G. Salvietti, D. Prattichizzo, "An EMG Interface for the Control of Motion and Compliance of a Supernumerary Robotic Finger," *Frontiers in Neurorobotics.*, vol. 10, pp. 18–30, 2016.

[7] Y. Sun, Z. Liu, and G. Yu, "An IMU/UWB Fusion Positioning Algorithm Based on a Particle Filter," *ISPRS International Journal of Geo-Information.*, vol. 6, pp. 235–247, 2017.

[8] T. Moore, D. Stouch, "A generalized extended kalman filter implementation for the robot operating system," *Proceedings of the 13th International Conference IAS-13.*, vol. 13, pp. 335–348, 2016.

[9] T. Nguyen, A. H. B. Zaini, C. Wang, K. Guo, L. Xie, "Robust Target-Relative Localization with Ultra-Wideband Ranging and Communication," *IEEE international conference on robotics and automation (ICRA).*, vol. 13, pp. 2312–2319, 2018.

[10] R. Leishman, J. Macdonald, T. McLain, R. Beard, "Relative navigation and control of a hexacopter," *IEEE International Conference on Robotics and Automation.*, vol. 1, pp. 4937-4942, 2012.

[11] M. Camurri, M. Ramezani, S. Nobili, M. Fallon, "Pronto: A Multi-Sensor State Estimator for Legged Robots in Real-World Scenarios," *Frontiers in Robotics and AI.*, vol. 7, pp. 68-79, 2020.

[12] S. Mishra, G. Pandey, S. Saripalli, "Target-free Extrinsic Calibration of a 3D-Lidar and an IMU," *IEEE International Conference on Multisensor Fusion and Integration for Intelligent Systems (MFI).*, vol. 1, pp. 1-7, 2021.

[13] AM. Lehrmann, PV. Gehler, S. Nowozin, "Efficient Nonlinear Markov Models for Human Motion," *Proceedings of the IEEE Conference on Computer Vision and Pattern Recognition (CVPR).*, vol. 1, pp. 1314-1321, 2014.

[14] P. Maurice, A. Malais, C. Amiot, N. Paris, G. Richard, O. Rochel, S. Ivaldi, "Human movement and ergonomics: An industry-oriented dataset for collaborative robotics," *The International Journal of Robotics*
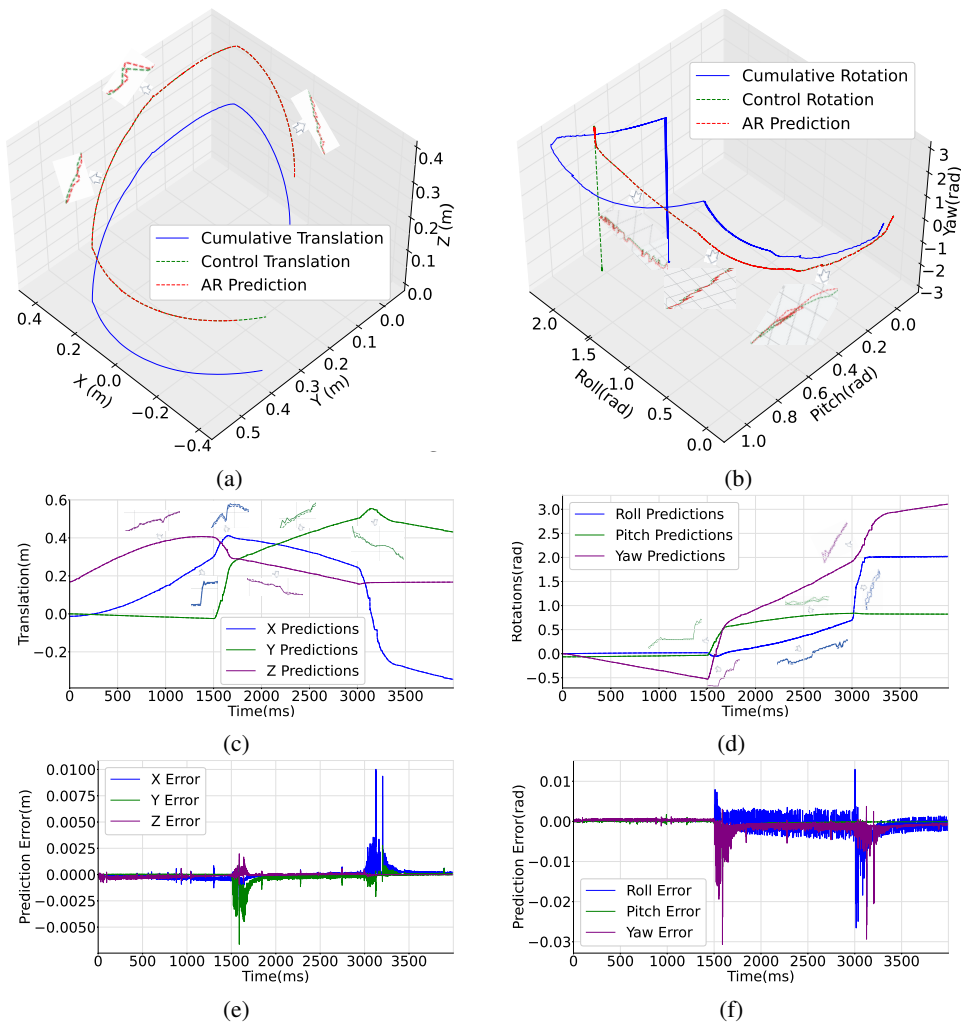
Fig. 10: (a)-(b) depict the 3D relationship between control inputs and the SRL's end-effector deformations in translation and rotation. (c)-(d) detail the breakdown of translational and rotational deformation predictions against control inputs, with dashed lines representing original inputs and solid lines indicating predictions. (e)-(f) analyze prediction errors over time for both translation and rotation.

Research., vol. 38, pp. 1529-1537, 2019.

[15] J. Luo, D. Huang, Y. Li, C. Yang, "Trajectory Online Adaption Based on Human Motion Prediction for Teleoperation," *IEEE Transactions on Automation Science and Engineering.*, vol. 19, pp. 3184-3191, 2021.

[16] M. Rubagotti, T. Taunyazov, B. Omarali, A. Shintemirov, "Semi-Autonomous Robot Teleoperation With Obstacle Avoidance via Model Predictive Control," *IEEE Robotics and Automation Letters.*, vol. 4, pp. 2746-2753, 2019.

[17] Y. Chen, U. Rosolia, W. Ubellacker, N. Csomay-Shanklin, A. Ames, "Interactive Multi-Modal Motion Planning With Branch Model Predictive Control," *IEEE Robotics and Automation Letters.*, vol. 7, pp. 5365-5372, 2022.

[18] C. Davenport, F. Parietti, HH. Asada, "Design and biomechanical analysis of supernumerary robotic limbs," *Dynamic Systems and Control Conference.*, vol. 45295, pp. 787-793, 2012.

[19] S.-w. Leigh and pp. Maes, "Body integrated programmable joints interface," *Proceedings of the 2016 CHI Conference on Human Factors in Computing Systems.*, pp. 60536057, 2016.

[20] M. Al-Sada, T. Hglund, M. Khamis, J. Urbani, and T. Nakajima, "OROCHI: Investigating requirements and expectations for multipurpose daily used supernumerary robotic limbs," *Proceedings of the 10th Augmented Human International Conference.*, pp. 1-9, 2019.

[21] Y. Zhu, H. Shikida, T. Aoyama, and Y. Hasegawa, "Evaluating shifted body representation and modified body schema using extra robotic thumb," *2018 IEEE International Conference on Cyborg and Bionic Systems (CBS). IEEE*, pp. 282-285, 2018.

[22] M. Tsakiris and pp. Haggard, "The rubber hand illusion revisited: Visuotactile integration and self-attributio," *Journal of experimental psy-chology: Human perception and performance.*, vol. 31, no. 1, pp. 80, 2005.

[23] B. Llorens-Bonilla, F. Parietti, and H. H. Asada, "Demonstration-based control of supernumerary robotic limbs," *RSJ International Conference on Intelligent Robots and Systems* 2012, pp. 39363942.

[24] M. Iwaki, Y. Hasegawa, and Y. Sankai, "Study on wearable system for daily life support using mckibben pneumatic artificial muscle," *International Conference on Intelligent Robots and Systems. IEEE* , pp. 36703675, 2010.

[25] L. Treers, R. Lo, M. Cheung *et al.*, "Design and control of lightweight supernumerary robotic limbs for sitting/standing assistance," *International Symposium on Experimental Robotics. Springer International Publishing.*, pp. 299308, 2017.

[26] Y. Li, L. Yang, D. Huang, C. Yang, J. Xia, "A proactive controller for human-driven robots based on force/motion observer mechanisms," *IEEE Transactions on Systems, Man, and Cybernetics: Systems.*, vol. 52, no. 10, pp. 6211-6221, 2022.

[27] M. Wang, F. Ou, H. Shi, C. Yang, X. Liu, "Model-based adaptive event-triggered tracking control of discrete-time nonlinear systems subject to strict-feedback form," *IEEE Transactions on Systems, Man, and Cybernetics: Systems.*, vol. 52, no. 7, pp. 4557-4568, 2021.

[28] C. Yang, G. Peng, L. Cheng, J. Na, Z. Li, "Force sensorless admittance control for teleoperation of uncertain robot manipulator using neural networks," *IEEE Transactions on Systems, Man, and Cybernetics: Systems.*, vol. 51, no. 5, pp. 3282-3292, 2019.

[29] F. Wu and H. Asada, "Bio-Artificial Synergies for Grasp Posture Control of Supernumerary Robotic Fingers," *Univ. California at Berkeley, Berkeley, CA, USA, 2014*

[30] M. Hao, J. Zhang, K. Chen, H. Asada, C. Fu, "Supernumerary robotic limbs to assist human walking with load carriage," *Journal of Mechanisms and Robotics.*, vol. 12, no. 6, pp. 061014, 2020.

[31] DA. Kurek, HH. Asada, "The MantisBot: Design and impedance control of supernumerary robotic limbs for near-ground work," *IEEE International Conference on Robotics and Automation (ICRA).*, pp. 5942-5947, 2017.

[32] H. Zhu, X. Li, L. Wang, Z. Chen, Y. Shi, S. Zheng, M. Li, "IMU Motion Capture Method with Adaptive Tremor Attenuation in Teleoperation Robot System," *Sensors.*, vol. 22, pp. 33533363, 2022.

[33] G. kulj, R. Vrabi, pp. Podraj, "A wearable imu system for flexible teleoperation of a collaborative industrial robot," *Sensors.*, vol. 21, pp. 58715883, 2021.

[34] S. Li, J. Jiang, pp. Ruppel, H. Liang, X. Ma, N. Hendrich, F. Sun, J. Zhang, "A mobile robot hand-arm teleoperation system by vision and imu," *IEEE/RSJ International Conference on Intelligent Robots and Systems (IROS).*, pp. 10900-10906, 2020.

[35] FC. Weigend, S. Sonawani, M. Drolet, HB. Amor, "Anywhere: Human Arm Pose from Smartwatch Data for Ubiquitous Robot Control and Teleoperation," *arXiv preprint arXiv.*, 2306.13192, 2023.

[36] V. Girbs-Juan, V. Schettino, L. Gracia, JE. Solanes, Y. Demiris, J. Tornero , "Combining haptics and inertial motion capture to enhance remote control of a dual-arm robot," *Journal on Multimodal User Interfaces.*, pp. 1-20, 2022.

[37] S. Tortora, S. Michieletto, F. Stival, E. Menegatti, "Fast human motion prediction for human-robot collaboration with wearable interfaces," *IEEE International Conference on Cybernetics and Intelligent Systems (CIS) and IEEE Conference on Robotics, Automation and Mechatronics (RAM).*, pp. 457-462, 2019.

[38] Y. Qingni, Y. Junhui, S. Ruitong, B. Huan, "Path Planning of a Mechanical Arm Based on an Improved Artificial Potential Field and a Rapid Expansion Random Tree Hybrid Algorithm," *Algorithms.*, vol. 14, pp. 1129-1133, 2021.

[39] X. Yingqi, S. Wei, Z. Wen, L. Jingqiao, L. Qinhui, S. Han, "A real-time dynamic path planning method combining artificial potential field method and biased target RRT algorithm," *Journal of Physics: Conference Series.*, vol. 1905, n. 1, pp. 012015-012027, 2021.

[40] L. Luo, H. Wen, Q. Lu, H. Huang, W. Chen, X. Zou, C. Wang, "Collision-free path-planning for six-DOF serial harvesting robot based on energy optimal and artificial potential field," *Complexity.*, 2018.

[41] H. Zhu, X. Li, L. Wang, Z. Chen, Y. Shi, S. Zheng, M. Li, "IMU motion capture method with adaptive tremor attenuation in teleoperation robot system," *Sensors.*, vol. 22, pp. 3353, 2022.

[42] M. Muhammad J. Samodro, R. Puriyanto, W. Caesarendra, "Artificial Potential Field Path Planning Algorithm in Differential Drive Mobile Robot Platform for Dynamic Environment," *International Journal of Robotics and Control Systems.*, vol. 3, 2023.

[43] Q. Jiang, Kai Cai, Fengyu Xu, "Obstacle-avoidance path planning based on the improved artificial potential field for a 5 degrees of freedom bending robot," *Mechanical Sciences.*, vol. 14, pp. 87-97, 2023.

[44] M. Salman, H. Khan, MC. Lee, "Perturbation Observer-Based Obstacle Detection and Its Avoidance Using Artificial Potential Field in the Unstructured Environment," *Applied Sciences.*, vol. 13, pp. 943-956, 2023.

[45] MJ. Kim, D. Lim, G. Park, J. Park, "A model predictive capture point control framework for robust humanoid balancing via ankle, hip, and stepping strategie," *arXiv preprint.*, arXiv:2307.13243, 2023.

[46] S. Li, H. Wang, S. Zhang, "Human-robot collaborative manipulation with the suppression of human-caused disturbance," *Journal of Intelligent and Robotic Systems.*, vol. 73, pp. 102-113, 2021.

[47] N. Amirshirzad, A. Kumru, E. Oztop, "Human adaptation to humanrobot shared control," *IEEE Transactions on Human-Machine Systems.*, vol. 49, n. 2, pp. 126-136, 2019.

[48] J. Luo, Z. Gong, Y. Su, L. Ruan, Y. Zhao, HH. Asada, C. Fu, "Modeling and balance control of supernumerary robotic limb for overhead tasks," *IEEE Robotics and Automation Letters.*, vol. 6, n. 2, pp. 4125-4132, 2021.

[49] Z. Tu, Y. Fang, Y. Leng, C. Fu, "Task-based human-robot collaboration control of supernumerary robotic limbs for overhead tasks," *IEEE Robotics and Automation Letters.*, 2023.

[50] DJ. Gonzalez, HH. Asada, "Hybrid open-loop closed-loop control of coupled humanrobot balance during assisted stance transition with extra robotic legs," *IEEE Robotics and Automation Letters.*, vol. 4, n. 2, pp. 1676-1683, 2019.

[51] M. Versteyhe, HD. Vroey, F. Debrouwere, H. Hallez *et al.*, "A novel method to estimate the full knee joint kinematics using low cost IMU sensors for easy to implement low cost diagnostics," *Sensors.*, vol. 20, pp. 16831698, 2020.

[52] L. Pei, R. Guinness, R. Chen, J. Liu, H. Kuusniemi, Y. Chen, L. Chen, J. Kaistinen, "Human behavior cognition using smartphone sensors," *Sensors.*, vol. 13, pp. 1402-1424, 2013.

[53] M.Ribeiro, "Kalman and extended kalman filters: Concept, derivation and propertiess," *Institute for Systems and Robotics.*, vol. 46, pp. 3736-3741, 2004.

[54] J. Redmon, S. Divvala, R. Girshick, A. Farhadi, "You only look once: Unified, real-time object detection," *IEEE conference on computer vision and pattern recognition.*, vol. 13, pp. 779-788, 2016.

[55] J. Sola, J. Deray, D. Atchuthan, "A micro Lie theory for state estimation in robotics," *arXiv preprint.*, arXiv:1812.01537, 2018.

[56] KC. Veluvolu, WT. Ang, "Estimation of physiological tremor from accelerometers for real-time applications," *Sensors.*, vol. 11, n. 3, pp. 3020-3036, 2018.